Enhanced truncated-correlation photothermal coherence tomography with application to deep subsurface defect imaging and 3-dimensional reconstructions

Pantea Tavakolian, [iD] Koneswaran Sivagurunathan, and Andreas Mandelis

View Online   Export Citation   CrossMark

ARTICLES YOU MAY BE INTERESTED IN

CrossMark
click for updates

Enhanced truncated-correlation photothermal coherence tomography with application to deep subsurface defect imaging and 3-dimensional reconstructions

Pantea Tavakolian, Koneswaran Sivagurunathan, and Andreas Mandelis[a)]

Center for Advanced Diffusion-Wave and Photoacoustic Technologies (CADIPT), Department of Mechanical and Industrial Engineering, University of Toronto, Toronto, Ontario M5S3G8, Canada

Photothermal diffusion-wave imaging is a promising technique for non-destructive evaluation and medical applications. Several diffusion-wave techniques have been developed to produce depth-resolved planar images of solids and to overcome imaging depth and image blurring limitations imposed by the physics of parabolic diffusion waves. Truncated-Correlation Photothermal Coherence Tomography (TC-PCT) is the most successful class of these methodologies to-date providing 3-D subsurface visualization with maximum depth penetration and high axial and lateral resolution. To extend the depth range and axial and lateral resolution, an in-depth analysis of TC-PCT, a novel imaging system with improved instrumentation, and an optimized reconstruction algorithm over the original TC-PCT technique is developed. Thermal waves produced by a laser chirped pulsed heat source in a finite thickness solid and the image reconstruction algorithm are investigated from the theoretical point of view. 3-D visualization of subsurface defects utilizing the new TC-PCT system is reported. The results demonstrate that this method is able to detect subsurface defects at the depth range of ∼4 mm in a steel sample, which exhibits dynamic range improvement by a factor of 2.6 compared to the original TC-PCT. This depth does not represent the upper limit of the enhanced TC-PCT. Lateral resolution in the steel sample was measured to be ∼31 μm. *Published by AIP Publishing.* [http://dx.doi.org/10.1063/1.4992807]

I. INTRODUCTION

Active infrared thermography is a non-contact, fast, and reliable technique that has received growing attention for diagnostic and monitoring applications in the past two decades. Thermography has evolved as an imaging modality for applications previously addressed by other standard non-destructive evaluation (NDE) techniques like ultrasound, X-Ray, or eddy current. This technology has been increasingly used in aerospace, power generation, and automotive industry applications to detect both manufacturing and in-service environment-induced defects.[1–8] Thermal imaging is non-ionizing and non-invasive and is used in medical applications such as detection of early caries in teeth with better sensitivity than radiography[9–12] and bone imaging with the aim of establishing a diagnostic technique for osteoporosis.[13,14] In breast thermal imaging, an abnormal infrared image has been proven to be an effective marker for a high risk of developing breast cancer.[15–18]

Photothermal imaging methods are either in the time domain or in the frequency domain. For time-domain techniques, the resulting amplitude images are very prone to non-uniformities in applied excitation, ambient reflections, and sample surface conditions.[19] However, frequency domain techniques, such as Lock-In Thermography (LIT), Thermal-Wave Radar (TWR), and Truncated-Correlation Photothermal Coherence Tomography (TC-PCT), also give rise to phase images that are emissivity normalized and can

carry more information with more or less sensitivity and dynamic range. Thermal-wave phase is independent of illumination intensity non-uniformities and surface conditions.[19,20]

Detection of depth-integrated distributions of energy is an attribute of the parabolic nature of diffusion-wave fields, which results in poor axial resolution.[21] In thermal imaging, this is a serious limiting factor when 3-D visualization of the sample is required.[19,21] Several signal processing methods have been applied to the infrared data to achieve energy localization in a thermal wave field and to enhance the signal-to-noise ratio (SNR) of the infrared images.[9,21,22] Unlike LIT that utilizes single frequency thermal waves, the TWR modality benefits from an improved depth resolved capability owing to its multi-frequency character and is suited for subsurface probing. This is so because linear frequency modulation (LFM), or phase coding modulation excitation in radar, yields information from more than a single diffusion length. To detect a photothermal signal in a noisy channel with high SNR, the photothermal pulse compression technique was introduced in our laboratory 30 years ago[23–25] and has more recently been developed for thermophotonic imaging applications.[22,26,27] This technique computes the cross-correlation between a reference signal derived from the excitation waveform and the resulting photothermal signal. In another study in our laboratory,[13] a highly depth resolved chirped pulse photothermal radar was introduced. This study proved that among four distinct chirped excitation waveforms (sine-wave, square-wave, constant width, and constant duty cycle pulses) for pumping the laser under

a)mandelis@mie.utoronto.ca

constant exposure energy and chirp energy lower than 100 mJ, fixed-pulsewidth chirps of large peak power exhibit SNR improvement up to two orders of magnitude compared to all other equal energy modalities.[13]

The recently introduced TC-PCT pulsed-chirp PT radar[21] is, to our best knowledge, the most successful evolution of dynamic thermal imaging methodologies to-date, providing much improved SNR and depth profiling capabilities. TC-PCT uses a chirped pulse excitation with fixed pulse width, performs pulse-compression, and uses a time-evolving filter controlled by pulse delay and time slicing width. TC-PCT cross-correlates the thermal transient signals with the sliced and delay-shifted reference signal and reconstructs the depth distribution of photothermal parameters. The clear depth-resolved advantage of a TC-PCT system compared to other thermal imaging methods has motivated the present introduction of an enhanced instrumentation and image reconstruction algorithm, followed by a non-destructive imaging (NDI) application of an opaque solid (steel with subsurface drilled holes).

In this study, an optimized TC-PCT system and an optimized reconstruction algorithm compared to the original TC-PCT method[21] have been developed. A theoretical approach for modeling the behavior of the thermal transient signals generated from chirped pulse photothermal excitation in the steel sample has also been introduced. Experiments were performed on the steel sample with TC-PCT, LIT,[9] and TWR[22] in order to compare these different photothermal imaging methods. The TC-PCT system was found to be able to detect defects far beneath the effective detection range of the other modalities. The results also show improvements in lateral resolution by a factor of three compared to the original TC-PCT[21] by means of a high resolution camera. In the following sections, analytical solutions to the TC-PCT heat diffusion boundary-value problem for a pulsed-chirp excitation signal input, along with simulations, and experimental results are presented and discussed.

II. THERMAL-WAVE LFM SIGNAL GENERATION THEORY

A theoretical formalism is developed for photothermal heat diffusion in a homogeneous sample with a finite thickness. Considering the illumination beam size to be much larger than the thermal diffusion length, we assume a one-dimensional solution to the thermal-wave problem with boundary conditions of the third kind at the front and the rear surface of the sample, Eq. (1a)

$$\frac{d^2T(z,\omega)}{dz} - \frac{i\omega}{\alpha}T(z,\omega) = -\frac{1}{k}Q(z,\omega), \quad (1a)$$

$$k\frac{dT(z,\omega)}{dz}\bigg|_{z=0} = h_1 T(0,\omega), \quad (1b)$$

$$-k\frac{dT(z,\omega)}{dz}\bigg|_{z=L} = h_2 T(L,\omega). \quad (1c)$$

Following a spatial optical impulse excitation at $z=0$ and assuming an opaque solid with surface optical

absorption, the spectral element of the temperature of the sample of thickness L (the Green function Fourier transform) can be expressed in the frequency domain as in Eq. (2)[28]

$$G(z,\omega) = \frac{I}{2\alpha\sigma(\omega)}\frac{(1+B_1)\left(e^{-\sigma(\omega)z} + B_2 e^{-\sigma(\omega)[2L-z]}\right)}{1 - B_1 B_2 e^{-\sigma(\omega)2L}}, \quad (2)$$

where

$$B_1(\omega) = \frac{k\sigma(\omega) - h_1}{k\sigma(\omega) + h_1}, \quad B_2(\omega) = \frac{k\sigma(\omega) - h_2}{k\sigma(\omega) + h_2}, \quad \text{and}$$

$$\sigma(\omega) = (1+i)\sqrt{\frac{\omega}{2\alpha}}. \quad (3)$$

I is the intensity of the incident laser beam (W/m²). Here, α is the thermal diffusivity (m²/s) of the solid, k is the thermal conductivity (W/mK), Q is the volumetric harmonic source function (W/m³), h_1 and h_2 are the heat transfer coefficients (W/m² K) at the front and the rear steel air interface, and $\sigma(\omega)$ is the thermal wavenumber at angular frequency ω. Since the camera records the surface temperature of the optically opaque block, the temperature variation at $z=0$ is the desired quantity. Following a temporal impulse excitation, the resulting transient temperature distribution is obtained from the inverse Fourier transform of Eq. (2)[28]

$$T_{impulse}(0,t) = \frac{1}{2\pi}\int_{-\infty}^{\infty}G(0|0;\omega)e^{i\omega t}d\omega$$

$$= \frac{I}{2\alpha}\int_{-\infty}^{\infty}\frac{(1+B_1)\left(1+B_2 e^{-2\sigma(\omega)L}\right)}{\sigma(\omega)\left(1 - B_1 B_2 e^{-2\sigma(\omega)L}\right)}e^{i\omega t}d\omega. \quad (4)$$

This thermal-wave impulse response can be used to calculate any photothermal response to an arbitrary excitation waveform $E(t)$ through the convolution of the arbitrary signal with $T_{impulse}(0,t)$[21]

$$T_{arbitrary}(t) = E(t) * T_{impulse}(0,t). \quad (5)$$

In this study, the excitation signal is a LFM pulsed waveform

$$E(t) = \sum_{m=0}^{p}\delta\left[t - \left(\frac{-\omega_1 + \sqrt{\omega_1^2 + 2\pi r(4m+1)}}{2r}\right)\right], \quad (6)$$

where ω_1 is the starting angular frequency, $r = (\omega_2 - \omega_1)/T$ is the sweep rate, and $m = 0, 1, 2,...p$, where p+1 is the number of pulses to be generated. Here, ω_2 is the ending angular modulation frequency, and T is the period of the LFM chirp. δ is the Dirac delta function.

For a chirped pulsed excitation, the in-phase thermal transient distribution can be obtained as

$$T_{chirp-pulse}(t) = \left\{\sum_{m=0}^{p}\delta\left[t - \left(\frac{-\omega_1 + \sqrt{\omega_1^2 + 2\pi r(4m+1)}}{2r}\right)\right]\right\}$$

$$* T_{impulse}(t). \quad (7)$$

III. ENHANCED TC-PCT SIGNAL GENERATION AND RECONSTRUCTION ALGORITHM

In the enhanced TC-PCT technique, the function generator produces a LFM pulsed chirp that controls the laser beam. The pulsed chirp excitation waveform is recorded by a data acquisition module for synthesizing the truncated reference chirp. The same synthesizing method introduced in the original TC-PCT system[21] is utilized to generate the in-phase reference truncated signal (R_0) and its quadrature (R_{90}) from the recorded excitation chirp

$$R_0(t) = \sum_{m=0}^{p} \int_{m}^{m+w_T} \delta\left[t - \left(\frac{-\omega_1 + \sqrt{\omega_1^2 + 2\pi r(4m+1)}}{2r}\right) - W_T\right]$$
$$\times \, dW_T, \tag{8}$$

$$R_{90}(t) = \sum_{m=0}^{p} \int_{m}^{m+w_T} \delta\left[t - \left(\frac{-\omega_1 + \sqrt{\omega_1^2 + 8m\pi r}}{2r}\right) - W_T\right] dW_T. \tag{9}$$

Axial resolution in the 3-D TC-PCT image of the sample depends on the time gate (W_T) specified in Eqs. (8) and (9). The minimum value for the W_T is limited by the camera frame rate, and the maximum is limited by the time difference between the last two pulses in the up-chirp waveform. Selecting a large time gate leads to a lower axial resolution, while it localizes more energy within the slice thickness thus leading to higher SNR.

A schematic diagram of the TC-PCT reconstruction algorithm, reference waveforms, and a thermal response signal are shown in Fig. 1. The procedure converts the excitation waveform to a square–wave chirp and then transmits the output through a delay-incremented unit ($C_{1f,0}$). Afterwards, the delay-incremented square-chirp is passed through a

frequency doubler ($C_{2f,0}$). Next, the delay-incremented square-chirp ($C_{1f,0}$) and its doubled frequency waveform ($C_{2f,0}$) are subjected to the binary exclusive-OR (EX-OR) operation to generate a quadrature square chirp. Truncated references R_0 and their quadrature R_{90} are then synthesized from $C_{1f,0}$ and $C_{1f,90}$, respectively.

The reconstruction of the thermal relaxation signals is based on the match filtering technique well-known in radar science.[13,21,29,30] As mentioned before, the delay-incremented unit shifts the in-phase/quadrature reference signals and generates different reference chirps ($R_{n,0}$ and $R_{n,90}$, n = 1, 2,...,q), Fig. 1(b). The technique, then, cross-correlates the in-phase and the quadrature of the reference chirp ($R_{n,0}$ and $R_{n,90}$) with the photothermal images (S_n) captured by the camera in a pixel-by-pixel format

$$CC_{n;0/90}(t) = \int_{-\infty}^{\infty} R_{n;0/90}^*(t+\tau) T_{chirp-pulse}(\tau) d\tau. \tag{10}$$

For fast calculations, the cross-correlation is executed in the frequency domain. Finally, the cross-correlation amplitude and phase can be calculated from

$$A_{CC,n} = \sqrt{CC_{n,0}^2 + CC_{n,90}^2}, \tag{11}$$

and

$$\varnothing_{cc,n} = \tan^{-1}\left(CC_{n,90}/CC_{n,0}\right). \tag{12}$$

In our analysis, the amplitude peak value is measured from the cross-correlation amplitude, Eq. (11). From the cross-correlation phase, Eq. (12), the phase value at the amplitude peak time provides the phase of one pixel. To obtain truncated information from the full cross-correlation, the original TC-PCT program searches for the peak in the first half of the
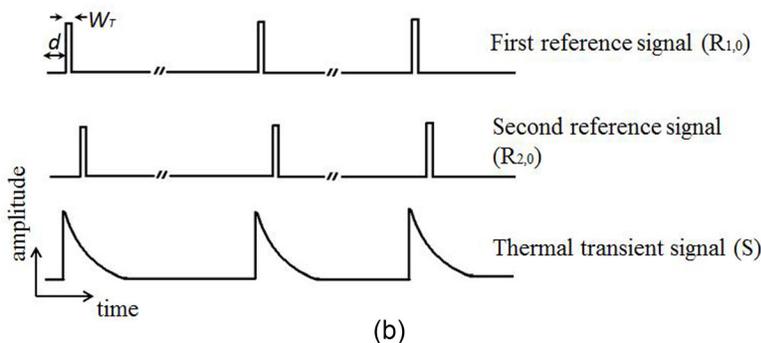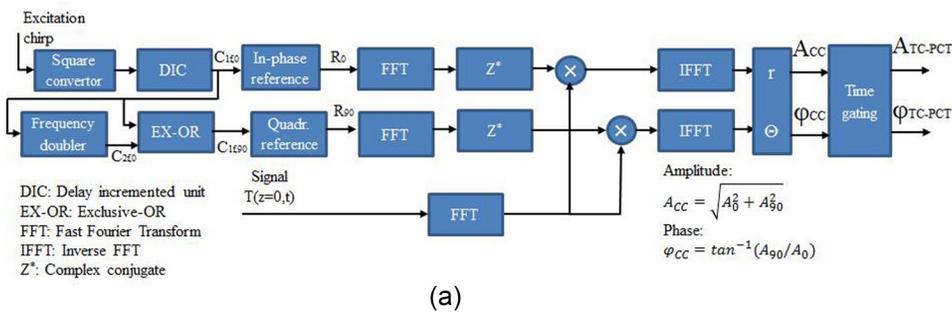

FIG. 1. (a) Enhanced TC-PCT reconstruction algorithm and amplitude and phase measurements; (b) an example of the shape of the first and the second truncated reference pulses ($R_{1,0}$, and $R_{2,0}$), and the photothermal chirp signal (S). The time scales for reference signals are not the same as the thermal transient signal; they are exaggerated so as to show the duration of the optical pulse.

amplitude and phase results. The enhanced TC-PCT program, however, searches for the amplitude peak based on the distance between the last two consecutive pulses in the full duration of the excitation signal waveform and is based on the following formula for the applied delay to the reference signals:

$$Time\ gating\ width = Shortest\ pulse\ distance - (n-1) \times d,$$
(13)

where n is the slice number and d is the delay applied to the reference signal, shown in Fig. 1(b). From the resulting cross-correlation amplitude, the time corresponding to the peak value of the cross-correlation produces the amplitude delay information. From the resulting cross-correlation phase, the time corresponding to zero phase value provides the phase delay data of one pixel. The time corresponding to the zero phase value specifies the net thermal flux of zero. This information provides the zero-delay phase TC-PCT of a sample and physically corresponds to the energy confinement within the delay-time slice. For all pixels of the captured photothermal images, the truncation process provides tomographic slice TC-PCT amplitude, amplitude peak delay time, phase, and zero-delay phase planar images (tomograms) of an optically excited solid. The time delay control represented by the time evolving filter W_T imparts spatial coherence to the resulting tomograms, a feature that is absent from conventional diffusion-controlled depth integrated photothermal imaging.

In summary, the major differences between the enhanced and original TC-PCT image reconstruction algorithms[21] are as follows: First, the enhanced modality is able to control the width of the truncated pulse such that, by increasing the pulse width, more energy can be localized within the slice for imaging deep structures with sufficient SNR. However, the axial resolution decreases when increasing the pulse width of the reference signal. Next, the phase images in the enhanced TC-PCT method are measured at the instant of the amplitude peak, while the original TC-PCT measures the minimum phase value. Finally, due to different time gating of the cross-correlation slices in the original TC-PCT, deep TC-PCT tomograms contained a mixture of information from both shallow and deep regions. The enhanced TC-PCT reconstruction algorithm filters the amplitude, Eq. (11), and the phase, Eq. (12), outputs using the windowing width shown in Eq. (13). Overall, compared to the original TC-PCT method, the enhanced TC-PCT modality is more precise in providing time resolved thermal information of the sample in a layer-by-layer manner.

IV. TC-PCT INSTRUMENTATION

In the TC-PCT experimental setup (Fig. 2), the excitation source is a pulsed diode laser (Jenoptic JOLD-120-QPXF-2P) connected to a laser driver (PCO-6131, Directed Energy, Colorado, USA) that is controlled by a function generator (Keysight 33500B, USA). The laser output is coupled to an optical fiber and passes through a collimator (F22SMA-B, Thorlabs Inc., New Jersey, USA) and a diffuser
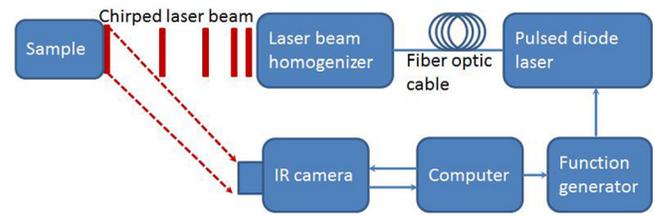

FIG. 2. Experimental setup for truncated-correlation photothermal coherence tomography (TC-PCT).

(ED1-C20, Thorlabs Inc., New Jersey, USA) to become intensity-homogenized before irradiating a sample. A 3–5 μm spectral band IR camera (A6700sc, FLIR, USA) captures the emitted radiation from the sample surface. A computer controls the entire system by executing the experimental TC-PCT algorithm in the LabView software. Compared to the original TC-PCT system,[21] the present improved system has a more sensitive camera and a state-of-the-art function generator that can generate a pulse chirp. Therefore, the original custom-built Schmitt trigger circuit and the pulse synthesizer, which were used for conversion of the chirp sine-wave to the pulse chirp-wave, were no longer needed, which makes the system instrumentation simpler.

The camera covers an area of 2.1 cm $\times$ 1.68 cm (sub-window: 1.1 cm $\times$ 0.88 cm) with a lateral resolution of 33 μm. It records a video on its own buffer in the FLIR format (ResearchIR Max 4, V.4.20.2, USA). Each frame of the video is exported as ASCII text files containing the data for each image pixel; then they are imported in the LabView environment. Subsequently, the camera frames are synchronized with the corresponding excitation signal recorded by a high speed data acquisition module (NI PCI-5122) and a post-processing algorithm reconstructs TC-PCT images from the IR frames recorded by the camera.

V. OPAQUE SOLID SUBSURFACE IMAGING

In our experiments, we studied an AISI 1010 steel block (6 cm $\times$ 4.5 cm $\times$ 3 cm) that had seven drilled subsurface holes (h_1-h_7), all with a diameter of 5 mm, at depths 400 μm, 600 μm, 1 mm, 1.5 mm, 3 mm, 3.5 mm, and 4 mm beneath its surface, Fig. 3. The thermal diffusivity and conductivity of the steel were 1.26 $\times$ 10^{-5} m^2/s and 49.8 W/mK, respectively.[31]

For the detection of the shallow holes (h_1-h_5), the sample surface was illuminated by a pulse chirp wave with a sweep range of 0.2–0.6 Hz, a duration of 12 s, and pulse durations of 10 ms, 30 ms, and 60 ms. The chirp beam with the pulse duration of 60 ms, 30 ms, and 10 ms was applied to holes h_5, h_4, and h_{1-3}, respectively. The laser beam illuminating the sample surface had a diameter of 3 cm, and the beam fluences for h_{1-3}, h_4, and h_5 were 7 mJ/cm^2, 63.6 mJ/cm^2, and 246 mJ/cm^2, respectively. The camera captured a series of frames covering an area of 2 cm $\times$ 1.68 cm on the steel surface, each image including one hole located almost at the center of the frame. The images were then reconstructed with the enhanced TC-PCT algorithm.

For detection of the two deepest holes (h_6 and h_7), the illumination parameters were changed to a pulse chirp wave
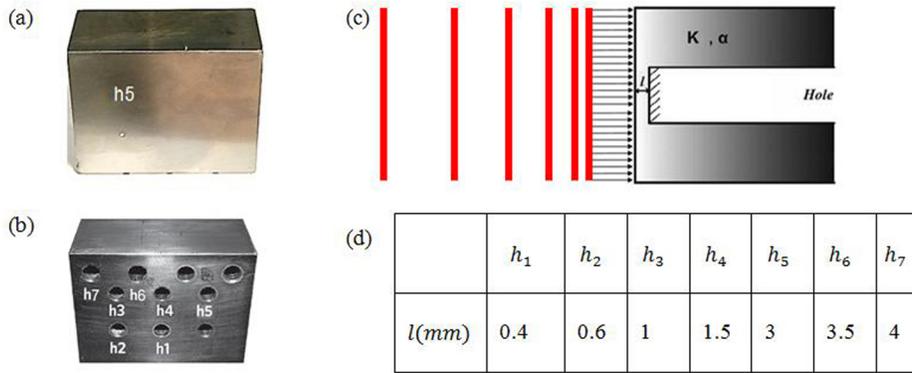
FIG. 3. Photograph of front surface (a) and back surface (b) of a steel sample with several blind holes at various depths. (c) Geometry of an opaque and semi-infinite solid sample (cross-section of one of the holes), the surface of which is uniformly illuminated by a chirped pulsed light beam. The front surface of the block was uniformly illuminated by a pulsed chirp laser beam. (d) Table of hole thicknesses. The steel block had an area of $45\,mm \times 60\,mm$ with a thickness of $30\,mm$. The diameter of all the holes was $5\,mm$.

with a sweep range of 0.08–0.6 Hz, a period of 27 s, and a pulse width of 250 ms. The starting frequency of the sweep was brought down to 0.08 Hz to increase the thermal penetration depth, since the thermal diffusion length ($\mu = \sqrt{2\alpha/\omega}$) is inversely proportional to the square root of frequency. For these experiments, increased light intensity was achieved by increasing the excitation pulse width and decreasing the diameter of the laser beam (2.5 cm). The camera covered an area of $1.1\,cm \times 0.88\,cm$ on the steel surface, again, with one hole located almost at the center of the frame. The light fluence to which the sample was exposed by the pulse chirp for the complete wave duration was $10.54\,J/cm^2$. For all the holes, three sets of data under identical experimental conditions were averaged to produce each TC-PCT image.

To compare the TC-PCT method with other thermal-wave imaging methods, experiments were performed and thermal images of the holes were reconstructed using LIT[9] and conventional TWR[22] imaging. LIT and TWR reconstruction algorithms used in this study are described elsewhere.[9,22] The illumination parameters for LIT were a square-wave beam with a duty cycle of 50% and a duration of 12-s at single frequencies of 0.2 Hz, 0.4 Hz, and 0.6 Hz. For TWR imaging, a square-wave beam with a duty cycle of 50%, a sweep range of 0.2 Hz to 0.6 Hz, and a duration of 12-s illuminated the steel sample. For these experiments, the laser beam diameter was 5 cm, and the camera frame size was $2\,cm \times 1.68\,cm$ on the steel sample, covering two holes in each frame. Although the laser beam power was reduced manually to one-third of the pulsed illumination, the light fluence to which the sample was exposed by the square wave was much higher than the energy used in the TC-PCT experiments for detection of the 3 mm hole ($10.68\,J/cm^2$ for the 0.2 Hz LIT experiment and $6.71\,J/cm^2$ for the TWR method).

VI. COMPUTATIONAL IMPLEMENTATION OF THE TC-PCT THEORY

As the laser illuminated a much larger area than the estimated thermal diffusion length, it was reasonable to assume a one-dimensional heat flow in the steel sample with a finite thickness. To simulate the photothermal transient signal, the 1-D solution for a pulsed excitation source, Eq. (4), was introduced. For different input excitation waveforms, for example, a pulse chirp beam, the transient temperature distribution was attained through the convolution of the optical source with the thermal transient response of the pulsed

excitation, Eq. (5). The simulation was executed in Matlab to generate photothermal signals from the holes and from the semi-infinite solid. Then, the thermal parameters of the solid were adjusted to best-fit the theoretical curves to the experimental data and the heat transfer coefficients of the holes were obtained.

The direct solution to the Green function for the thermal-wave boundary value problem described in Eqs. (1)–(3) for the pulse chirp excitation in the time domain is given elsewhere.[32] Since the time-domain solution requires eigenvalue calculations and eigenfunction expansions, the frequency domain solution based on Eq. (2) followed by inverse Fourier transformation was found to be much simpler and computationally less time consuming.

Transient temperature distributions in the steel plate of Fig. 3 with various thicknesses were simulated in Matlab software using Eq. (5). Adjusting the heat transfer coefficient, and using the thermal diffusivity and conductivity of the AISI 1010 steel sample,[31] the simulated thermal transient comb was made of a pulse chirp and was fitted to the experimental data with minimum 2.23% error, as shown in Fig. 4(a). Although two different heat transfer coefficients for the front (h_1) and the rear (h_2) surface of the steel were used in the formula, the calculated h values obtained for best fitting the front and the rear surface boundary conditions were the same and equal to $8.75\,W/m^2\,K$.

The cross-correlation expression, Eq. (10), was applied to both experimental and theoretical temperature transients. For a deeper insight into the cross-correlation behavior of the in-phase/quadrature reference signals, Fig. 4(b) shows in-phase and quadrature reference signals, with the in-phase and quadrature cross-correlations reconstructed in Matlab and provided in Figs. 4(c) and 4(d), respectively. The cross-correlation was performed in the frequency domain for fast computation, and the result is shown in the time domain using the inverse Fourier transformation. The delay time of the in/phase and quadrature reference signals, Fig. 4(b), cross-correlated with the thermal transient is zero, and the pulse width ($R_{1,0}$) is 9.6 ms. In this example, the in-phase reference pulses overlap the thermal peaks, which results in higher cross-correlation amplitude peak, Fig. 4(c), than the quadrature cross-correlation amplitude peak, Fig. 4(d). Amplitude and phase data for each pixel were measured from the cross-correlations using Eqs. (11) and (12).
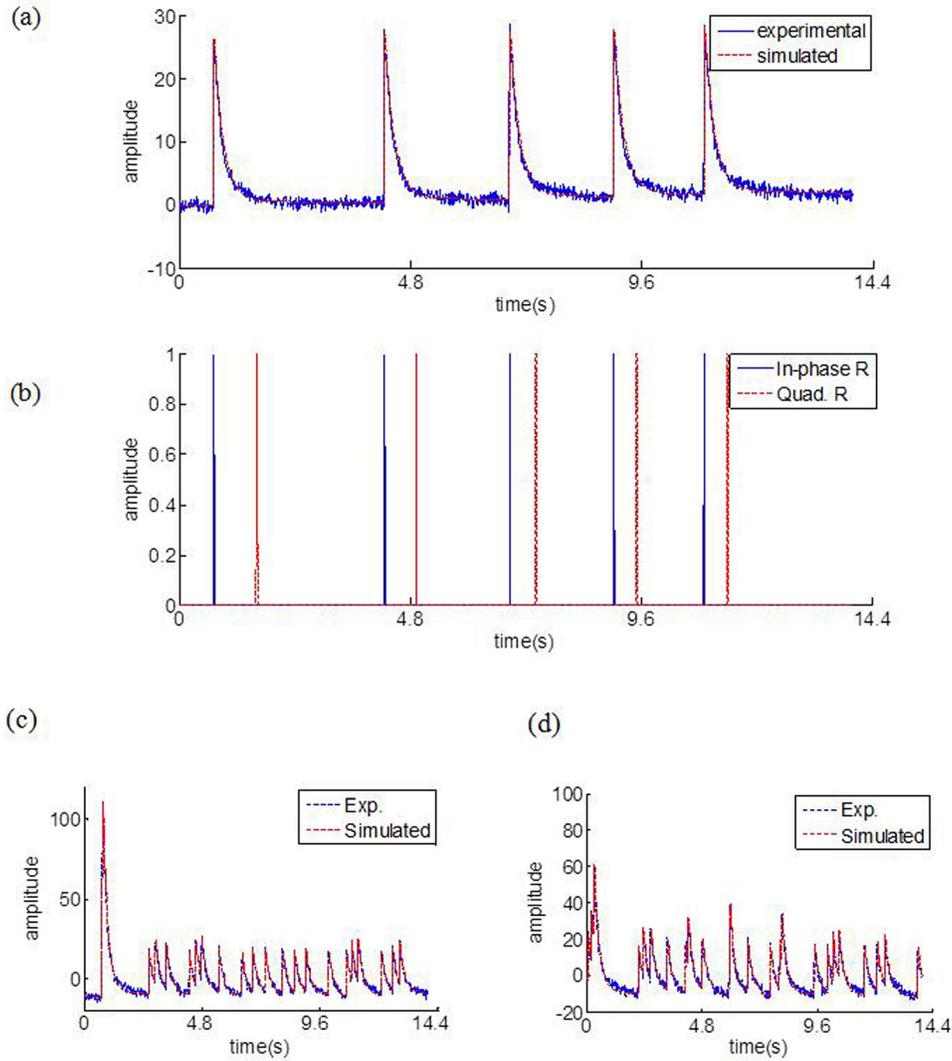
FIG. 4. TC-PCT theoretical analysis of photothermal transient signals. (a) Theoretical and experimental thermal transient signals corresponding to hole h_1. (b) In-phase and quadrature reference signals. Cross-correlation amplitudes of theoretical and experimental transients with in-phase (c) and quadrature (d) reference signals.

VII. TC-PCT EXPERIMENTAL IMAGE ANALYSIS

TC-PCT analysis provides four output channels: amplitude, peak delay time, phase, and zero-delay phase. The images of several subsurface holes in the steel block were captured and are displayed in Fig. 5. Each image represents an average of three images obtained under identical experimental conditions. All the planar images are taken after a delay time of 450 ms with a slice width (truncation) of 150 ms. The TC-PCT amplitude channel reveals significantly higher contrast than the phase channel in the case of shallow subsurface holes. However, for deeper holes than 1.5 mm, the amplitude channel becomes less sensitive, and eventually, it cannot detect the 3 mm, 3.5 mm, and 4 mm holes in the steel sample. The peak delay time, phase, and phase delay channels exhibit considerably higher dynamic range than the amplitude channel. The peak delay time channel does not provide as sharp a contrast between the hole and the semi-infinite substrate as the amplitude images in the case of shallow subsurface holes. For the deepest holes h_6 and h_7, the thermal energy accumulated at the back air interface of the solid layer measurably diffuses in radial directions away from the metal-air interface and therefore the size

of the hole is seen with a diameter somewhat larger than its actual size.

Figure 6 displays 3-D amplitude tomograms of h_1, h_2, and h_3 surrounded by the semi-infinite substrate. The 3-D images were reconstructed by stacking the planar image slices using ImageJ software.[33] These images are not on the same scale, and the software does not allow for associating quantitative amplitude value to image color in the volume viewing format. The 3-D images are reconstructed with 40 ms slice width and delay time. Each image covers an area of 2.1 cm × 1.68 cm on the sample, and the image time span is 1.2 s. Holes h_1 and h_2 are visible through the steel block as a consequence of the relatively high thermal diffusivity of steel, which makes the diffusion time of flight across the steel overlayer above h_1 and h_2 shorter than the temporal resolution of the camera. However, h_3 is axially resolved while the depth-profiling image contrast is decreased as a result of progressively significant signal attenuation. To estimate the mean diffusion depth corresponding to a given delay time following an impulsive thermal source on the surface of a semi-infinite solid, the following expression can be used based on the semi-infinite solid temperature impulse response:[29]
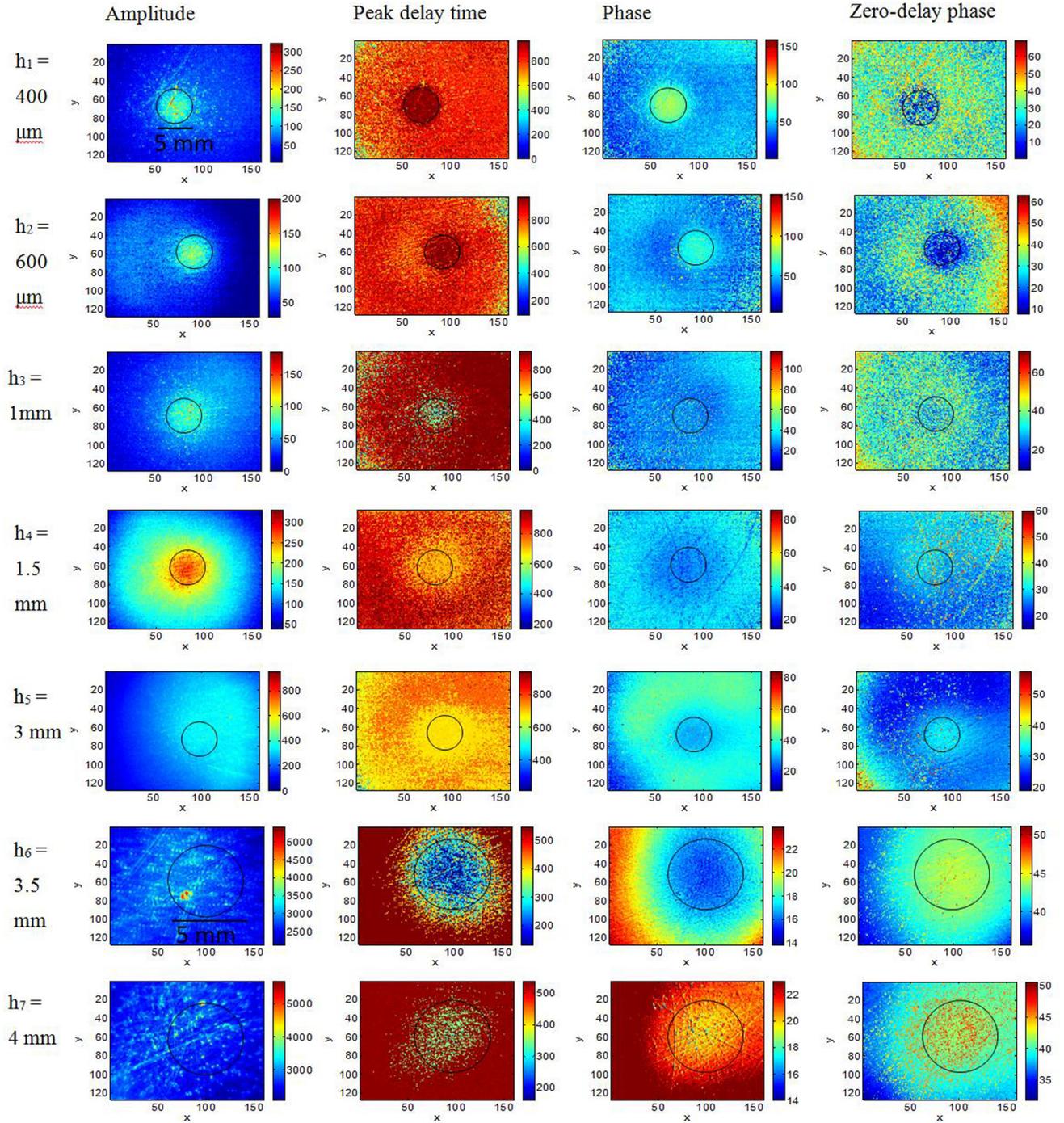
FIG. 5. Enhanced TC-PCT images of the steel sample. The steel block has seven holes, all with a diameter of 5 mm, at depths shown in Fig. 3. Each row displays four enhanced TC-PCT output channels (amplitude, peak delay time, phase, and zero-delay phase) for one of the holes. The black ring on each image shows the actual position of each hole. Images of holes h_{1-5} cover an area of 2.1 cm × 1.68 cm, and images of holes h_{6-7} cover an area of 1.1 cm × 0.88 cm on the steel surface. Therefore, in the TC-PCT images of h_{6-7}, the diameter of the black circle is two times that of the black circle in the h_{1-5} TC-PCT images. The truncation time gate is 150 ms for all the holes.

$$\bar{z} = \frac{\int_0^\infty z e^{-z^2/4\alpha t} dz}{\int_0^\infty e^{-z^2/4\alpha t} dz} = \frac{2\sqrt{\alpha t}}{\sqrt{\pi}}. \qquad (14)$$

This corresponds to 4.39 mm for 1.2 s image time span using 1.26×10^{-5} m²/s as the value for the thermal diffusivity of steel. The contrast between the hole and the substrate appears in all planar images along the z axis for h_1 and h_2. For the

deeper hole, h_3, however, contrast appears after the first (surface) tomogram (z = 0). The hole h_3 appears after 50 ms, which corresponds to 0.9 mm and is in good agreement with its actual depth location (1 mm). A and B marks on the images shown in Fig. 6 display the location of the hole and the energy accumulation at the back surface, respectively. The homogenized laser beam illuminating the block is at an angle with it, and consequently one side of it lies at a shorter distance to the laser than the other side. The temperature of the sample closer
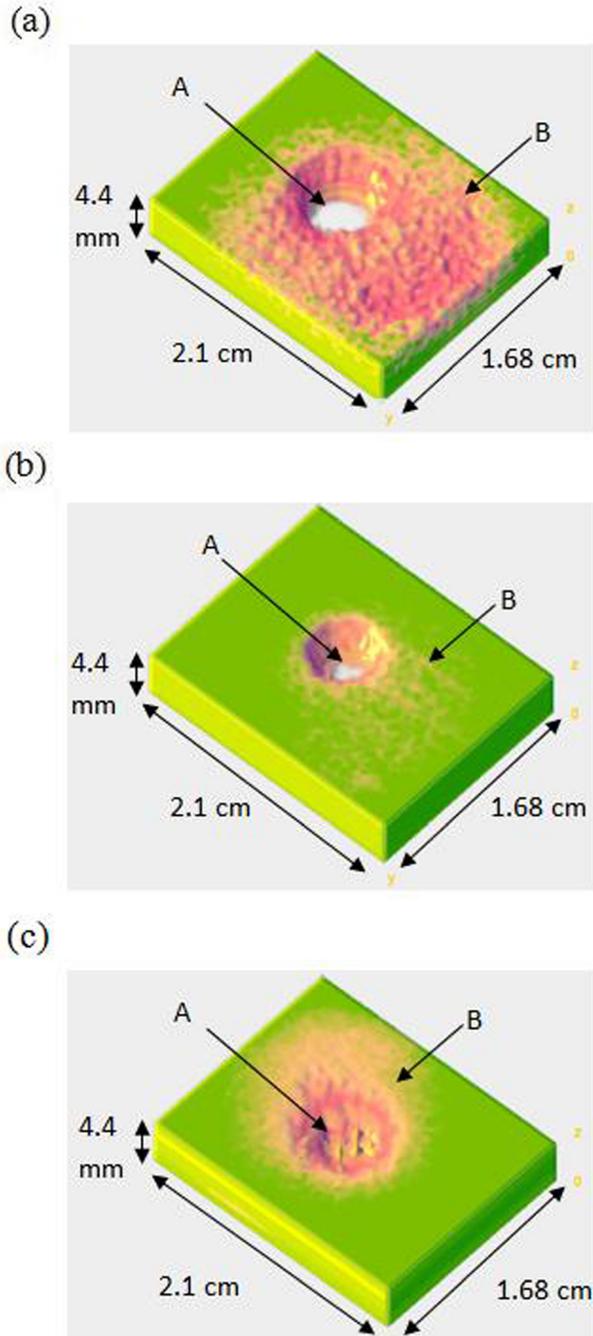
FIG. 6. 3-D visualization of the holes in the steel sample using TC-PCT imaging. Amplitude tomograms of the enhanced TC-PCT of hole h_1 (a), h_2 (b), and h_3 (c) with a truncation time gate of 40 ms. Each image covers an area of 2.1 cm × 1.68 cm on the sample, and the image delay time range is 1.2 s which corresponds to the depth of 4.39 mm. The $z = 0$ plane at the bottom of the image is the coordinate the camera recorded the thermal signals. A and B in these images display the holes and the energy accumulation at the back surface, respectively. The images of (a), (b), and (c) are not on the same scale. The laser beam illuminating the sample from the bottom is a pulsed chirped signal with a sweep range of 0.2 Hz–0.6 Hz, a duration of 12 s, and a pulse duration of 10 ms. The diameter of the illumination beam is 3 cm, and the laser intensity for the whole duration is 7 mJ/cm^2.

to the laser is higher, which can be observed in the accumulated energy in the 3-D images (B marks). The shallowest hole in Fig. 6(a) shows the largest sideways spread of the thermal-wave beyond the edges of the hole. This occurs because the mean thermal-wave amplitude is the highest for this hole

which corresponds to the strongest lateral temperature gradient and thus highest thermal-wave flux to the region outside the hole perimeter.

A 3-D phase-delay tomogram of a deep hole (h_6) is presented in Fig. 7. The first TC-PCT planar frame is reconstructed after 400 ms (pulse width = 250 ms and $W_T = 150$ ms), which corresponds to 2.53 mm. Nine 250-ms pulses illuminated the sample in the 27 s pulse duration. Therefore, the diffusing energy at the back surface was sufficient and had enough time to coherently accumulate up to the front surface and generate thermal-wave contrast. As a result, the contrast between the hole and the substrate appears right at the first frame. Since the subsurface hole was deep, the contrast between it and the semi-infinite substrate is low. Consequently, the differences between the thermal-wave amplitudes of these two adjacent regions are not noticeable in the last frames. The lateral diffusion spread is quite large in Fig. 7, rendering the effective size of the hole larger than its actual dimension. Unlike in Fig. 6(a), the reason for the large lateral thermal-wave spread is the longer diffusion time scale used to acquire this image while the lateral amplitude gradient is much weaker than that of Fig. 6(a).

The TC-PCT image of a 4-mm deep subsurface hole in steel, last row of Fig. 5, is, to our best knowledge, the deepest one ever obtained using a thermal-wave imaging method. For comparison of the TC-PCT method with conventional LIT and TWR, photothermal frames of the steel sample were captured and then reconstructed with these two methods. For LIT, three square-wave laser waveforms were used at 0.2 Hz, 0.4 Hz, and 0.6 Hz. Reconstruction of the LIT images with the 0.2 Hz square wave exhibited the best results for h_4, the deepest detected hole. For TWR, the sweep range spanned 0.2 Hz to 0.6 Hz, the same range as TC-PCT. 0.2-Hz square-wave LIT amplitude and phase images are displayed in Fig.
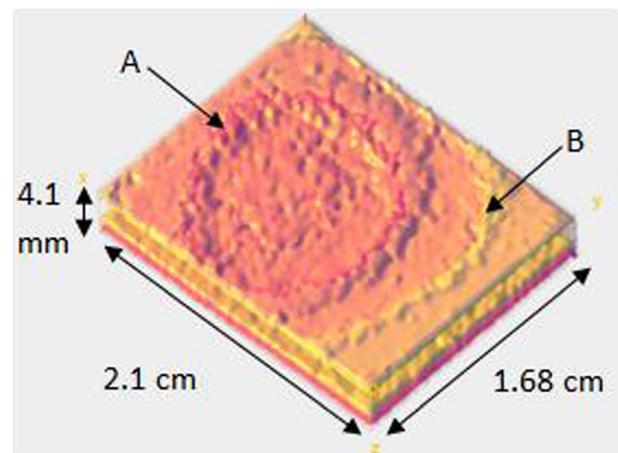

FIG. 7. 3-D visualization of phase-delay tomograms of enhanced TC-PCT of hole h_6 with truncation time gate of 150 ms. Each image covers an area of 1.1 cm × 0.88 cm on the sample, and the image delay time range is 1.05 s which corresponds to the depth of 4.1 mm. The $z = 0$ plane at the top of the image is the coordinate the camera recorded the thermal-wave signals. A and B on these images display the holes and the energy accumulation at the back surface, respectively. The laser beam illuminating the sample from the top generates a pulsed chirped signal with a sweep range of 0.08 Hz–0.6 Hz, a duration of 27 s, and a pulse duration of 250 ms. The diameter of the illumination beam is 2.5 cm, and the laser intensity for the whole duration is 10.54 J/cm^2.
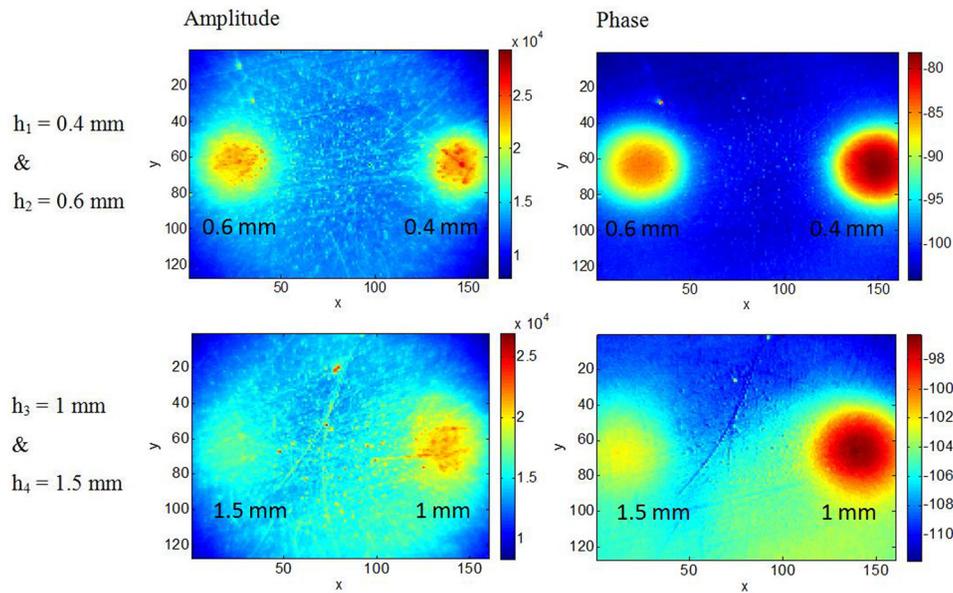
FIG. 8. Lock in thermography (LIT) amplitude and phase images of subsurface holes h_1 - h_4. Each image covers two holes. The beam used for capturing these images was a square-wave signal at a fixed frequency of 0.2 Hz, a duration of 12 s, and a pulse duration 10 ms. The diameter of the illumination beam was 5 cm, and the laser fluence was 10.68 J/cm^2. The LIT method was unable to detect holes deeper than 1.5 mm.

8, and TWR images are shown in Fig. 9. Each image is an average of three images under identical experimental conditions. Neither LIT nor TWR was capable of detecting any subsurface holes/defects beyond 1.5 mm beneath the surface. The LIT system could barely detect the 1.5 mm hole when 0.4 Hz and 0.6 Hz square-wave modulation was used. The 0.2 Hz square-wave not only provided a longer diffusion length but also delivered more illumination energy to the sample, which made it possible for LIT to detect the 1.5 mm hole.

VIII. DISCUSSION

In photothermal imaging, a modulated optical excitation signal heats a sample. In the back-propagation mode, a combination of the thermal infrared photon emission (radiation heat transfer) and conduction heat transport to the surface of the sample is detected by an infrared camera. In order to obtain depth resolved energy localization, several dynamic image reconstruction techniques are available using thermal transient relaxation signals. Among all inspection modalities in parabolic diffusion-wave fields to date, TC-PCT[21] provides the highest energy localization in a solid. TC-PCT has been modified since its inception and was improved in this work in terms of both instrumentation and reconstruction algorithm. The present enhanced TC-PCT has simpler instrumentation, a more advanced IR camera, exhibits dynamic range improvement by a factor of 2.6, and provides lateral resolution improvement by a factor of 3.0 in a steel sample.

As a non-destructive imaging (NDI) application, the TC-PCT modality was examined for imaging industrial materials with substructures (subsurface holes in steel) and it
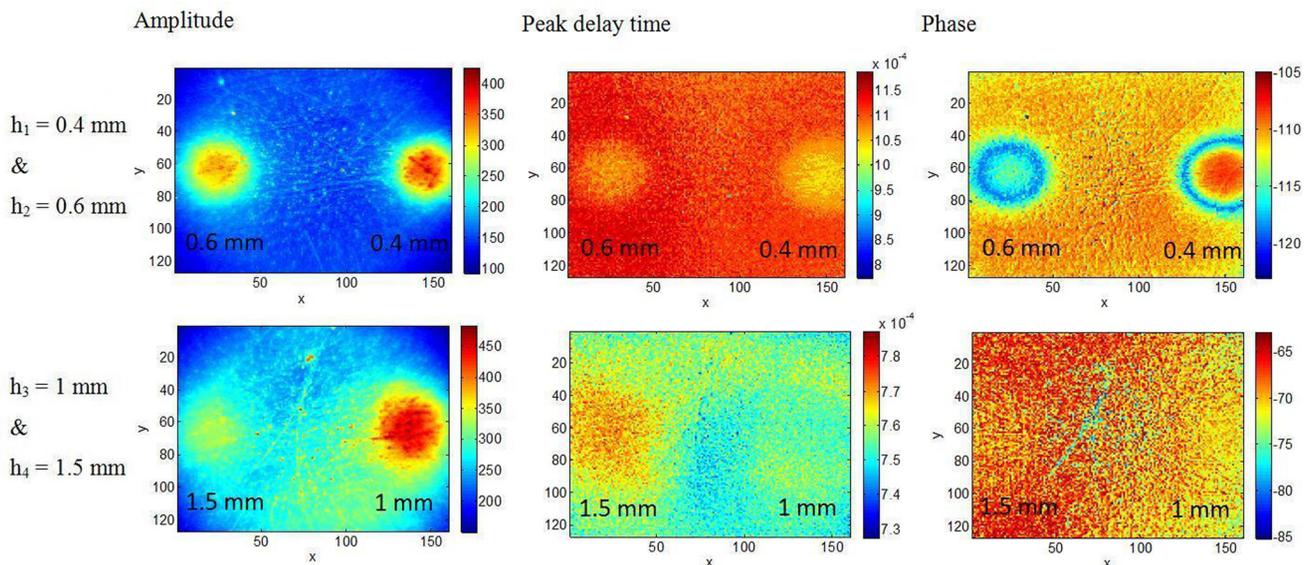

FIG. 9. Thermal-wave radar (TWR) amplitude, peak delay time, and phase images of subsurface holes h_1-h_4. Each image covers two holes. The beam used for capturing these images was a square-wave signal with a sweep range 0.2 Hz–0.6 Hz, a duration of 12 s, and a pulse duration of 10 ms. The diameter of the illumination beam was 5 cm, and the laser fluence was 6.71 J/cm^2. The TWR method was unable to detect holes deeper than 1.5 mm.

was demonstrated that this method exhibits considerable improvement in subsurface depth profiling/imaging capabilities over LIT and TWR. Holes h_1–h_7, which are resolved in the TC-PCT channels, have steel overlayer thicknesses of up to 4 mm, while LIT, TWR, and the original TC-PCT can only detect h_1–h_4 with the maximum overlayer thickness of 1.5 mm. For the deep holes, image contrast deteriorates due to progressively significant signal attenuation. The three deepest holes, h_5-h_7, cannot be detected with TC-PCT amplitude tomograms. The zero-delay phase channel provides information of locations within the sample where the net thermal flux is zero. This channel is particularly useful for biological tissue imaging where distributed optical absorption at different depths may occur inside the sample. It was found that in the case of deep subsurface holes, among the available signal channels (amplitude, phase, peak delay time, and zero-phase delay), the phase tomograms offer the highest dynamic range and sensitivity.

In TC-PCT, the limiting factor for axial resolution is the frame rate of the infrared camera. The delay applied to the reference signal with respect to the excitation chirp controls the depth range in the sense that it limits the frequency chirp repetition time which, in turn, determines the thermal diffusion length. To increase the depth range in TC-PCT imaging, one solution is applying a longer LFM chirp with lower starting frequency. In this study, to detect the deep holes in the steel sample, a longer chirp with a low starting frequency (0.08 Hz) was used. Another solution for an increase in depth range and image contrast is increasing the laser peak energy delivered to the sample.

IX. CONCLUSIONS

In this study, TC-PCT was optimized in terms of instrumentation and image reconstruction algorithm compared to the original TC-PCT method.[21] The enhanced TC-PCT modality was tested in a non-destructive imaging application to detect subsurface defects at various depths in a steel sample. A theoretical approach for the generation of the chirped pulse thermal transient signals and the resulting TC-PCT cross-correlations (in-phase and quadrature) in the steel sample was introduced. The enhanced TC-PCT images were experimentally compared with the original TC-PCT,[21] LIT,[9] and TWR[22] methods. Improvement in image lateral resolution by a factor of three was achieved compared to the original TC-PCT[21] images. The enhanced TC-PCT system was able to provide a dynamic range of 4 mm in the steel sample, the deepest to-date, and this is not an absolute detection limit. The original TC-PCT,[21] LIT,[9] and TWR[22] modalities were barely able to detect the 1.5 mm hole in the same steel sample. This technique has the potential to catalyze new venues of non-destructive photothermal and biomedical imaging

due to its versatility, sharp 3-D image generation using a diffusion-wave field, and deep subsurface penetration ability.

[1] J. A. Siddiqui, V. Arora, R. Mulaveesala et al., Exp. Mech. **55**, 1239 (2015).
[2] S. Ranjit, K. Kang, and W. Kim, Int. J. Precis. Eng. Manuf. **16**, 2255 (2015).
[3] S. Ranjit, M. Choi, and W. Kim, J. Mech. Sci. Technol. **30**, 1111 (2016).
[4] J. Yanga, S. Hwanga, Y. K. Anb, K. Leec, and H. Sohnaa, J. Mater. Process. Technol. **229**, 94 (2016).
[5] S. S. Pawar and V. P. Vavilov, Int. J. Heat Mass Transfer **94**, 56 (2016).
[6] R. Velazquez-Hernandez, A. Melnikov, A. Mandelis, K. Sivagurunathan, M. E. Rodriguez-Garcia, and J. Garcia, NDT&E Int. **45**, 16 (2012).
[7] X. Guo, K. Sivagurunathan, J. Garcia, A. Mandelis, S. Giunta, and S. Milletari, Appl. Opt. **48**, C11 (2009).
[8] J. Y. Liu, J. L. Gong, and L. Qin, Int. J. Thermophys. **36**, 1226 (2015).
[9] N. Tabatabaei, A. Mandelis, and B. T. Amaechi, J. Biomed. Opt. **16**, 071402 (2011).
[10] J. Jan, W. Z. Wan Bakar, S. M. Mathews, L. O. Okoye, B. R. Ehler, C. Louden, and B. T. Amaechi, J. Invest. Clin. Dent. **7**, 383 (2016).
[11] J. D. Silvertown, B. Y. Wong, K. S. Sivagurunathan, S. H. Abrams, J. Kirkham, and B. T. Amaechi, J. Invest. Clin. Dent. 12257 (2017).
[12] J. D. Silvertown, B. Y. Wong, S. H. Abrams, K. S. Sivagurunathan, S. M. Mathews, and B. T. Amaechi, J. Invest. Clin. Dent. 12239 (2016).
[13] S. Kaiplavil and A. Mandelis, Rev. Sci. Instrum. **82**, 074906 (2011).
[14] S. Kaiplavil and A. Mandelis, Int. J. Thermophys. **34**, 1481 (2013).
[15] M. Gautherie and C. M. Gros, Cancer **45**, 51 (1980).
[16] J. Koay, C. Herry, and M. Frize, Conf. Proc. IEEE Eng. Med. Biol. Soc. **2**, 1159 (2004).
[17] S. Ciatto, M. Rosselli Del Turco, S. Cecchini, G. Grazzini, and A. Iossa, Tumori **75**, 110 (1989).
[18] A. Lashkari, F. Pak, and M. Firouzmand, J. Med. Signals Sens. **6**, 12 (2016).
[19] A. Mandelis, Phys. Today **53**(8), 29 (2000).
[20] G. Busse, Appl. Phys. Lett. **35**, 759 (1979).
[21] S. Kaiplavil and A. Mandelis, Nat. Photonics **8**, 635 (2014).
[22] N. Tabatabaei and A. Mandelis, Rev. Sci. Instrum. **80**, 034902 (2009).
[23] A. Mandelis, Rev. Sci. Instrum. **57**, 617 (1986).
[24] A. Mandelis, L. M. L. Borm, and J. Tiessinga, Rev. Sci. Instrum. **57**, 622 (1986).
[25] A. Mandelis, L. M. L. Borm, and J. Tiessinga, Rev. Sci. Instrum. **57**, 630 (1986).
[26] R. Mulaveesala, J. S. Vaddi, and P. Singh, Rev. Sci. Instrum. **79**, 094901 (2008).
[27] G. Silipigni, P. Burrascano, D. A. Hutchins, S. Laureti, R. Petrucci, L. Senni, L. Torre, and M. Ricci, NDT&E Int. **87**, 100 (2017).
[28] A. Mandelis, Diffusion-Wave Fields: Mathematical Methods and Green Functions (Springer Science, New York, 2001), pp. 45–47.
[29] S. Kaiplavil, A. Mandelis, X. Wang, and T. Feng, Biomed. Opt. Express **5**, 2488 (2014).
[30] N. Tabatabaei and A. Mandelis, Phys. Rev. Lett. **107**, 165901 (2011).
[31] B. Boardman, Properties and Selection: Irons, Steels, and High-Performance Alloys (ASM International, USA, 1990), p. 1.
[32] K. D. Cole, J. V. Beck, A. Haji-Sheikh, and B. Litkouhi, Heat Conduction Using Green's Functions, 2nd ed. (Taylor & Francis Group, USA, 2010), p. 606.
[33] See http://rsb.info.nih.gov/ij/ for ImageJ.